Materials Today Bio 31 (2025) 101525

Contents lists available at ScienceDirect

Materials Today Bio

journal homepage: www.journals.elsevier.com/materials-today-bio

Adhesive micro-liquid for efficient removal of bacterial biofilm infection

Ying Wang [a], Zhibang Li [a], Lingli Ji [a], Jiao Sun [a], Fei Gao [a], Ruiqing Yu [a], Kai Li [a], Wenjun Wang [a], Weiwei Zhao [a,**], Qi-Zhi Zhong [b,***], Shaohua Ge [a], Jianhua Li [a,*]

[a] Department of Biomaterials, School and Hospital of Stomatology, Cheeloo College of Medicine, Shandong University & Shandong Key Laboratory of Oral Tissue Regeneration & Shandong Engineering Research Center of Dental Materials and Oral Tissue Regeneration & Shandong Provincial Clinical Research Center for Oral Diseases, Jinan, 250012, China

[b] School of Chemistry, Chemical Engineering and Biotechnology, Nanyang Technological University, 21 Nanyang Link, 637371, Singapore

ARTICLE INFO

Keywords:
Adhesion
Metal phenolic network
Bacterial infection
Ionic liquid
Assembly

ABSTRACT

Bacteria are common infectious pathogens that can cause invasive and potentially life-threatening infections. Ionic liquids have emerged as a novel class of alternatives to antibiotics, however their inherent hydrophobicity and immiscible in water exhibits poor adhesion to bacteria and diminishes its utilization and bioavailability for infection control. Herein, an adhesive metal phenolic encapsulated ionic liquid choline and geranate (CAGE@MPN) microcapsules is designed to address the aforementioned challenges and remove bacterial biofilm infections. The CAGE@MPN microcapsules are prepared through self-assembly of quercetin and ferrous ions on the interface of CAGE and water *via* metal-phenolic coordination. The MPN interface can stabilize the micro liquid and effectively adhere to bacterial surfaces. The microcapsules can disrupt bacterial cell walls to facilitate the release of cellular contents and destruct the biofilm, thereby exerting a pronounced bactericidal effect. The *in vivo* bactericidal effect of CAGE@MPN microcapsules is demonstrated in a murine model of *Staphylococcus aureus* (*S. aureus*) skin infection. The proposed adhesive micro-liquid system offers a promising strategy for noninvasive and efficient removal of bacterial biofilm infection.

1. Introduction

Bacterial infections have emerged as a significant global public health concern, associated with high morbidity rates, substantial mortality and long-term complications [1,2]. Invasive bacterial infections can lead to severe diseases and in some cases, become life-threatening [3–6]. Despite the ongoing development of new antibiotics and antibiotic adjuvants, bacteria can develop resistance in a relatively short period of time, posing significant therapeutic challenges. Therefore, it is essential to explore and develop innovative strategies for the effective management of bacterial infections [7–9].

Staphylococcus aureus (*S. aureus*), as a Gram-positive bacterium, is a common cause of both hospital-acquired and community-associated infections, such as boils and impetigo, pneumonia, osteomyelitis, endocarditis, and sepsis. Compared to mammalian cells, *S. aureus* has an additional dense cell wall outside its cell membrane, which is composing of glucans, chitin, mannans, and glycoproteins. The components form a cross-linked, multi-layered structure, providing structural integrity and posing a significant barrier to the penetration of antimicrobial agents [10,11]. Bacteria within biofilms exhibit altered metabolic states, which reduce their susceptibility to antimicrobial agents, and can exchange resistance genes more readily, contributing to the persistence of chronic

Abbreviations: S. aureus, *Staphylococcus aureus*; ILs, ionic liquids; CAGE, choline and geranate; MPNs, metal phenolic networks; Que, quercetin; LMCT, ligand-to-metal charge transfer; CLSM, confocal laser scanning microscope; NR, Nile Red; FTIR, fourier transform infrared spectroscopy; QCM, quartz crystal microbalance; SEM, scanning electron microscope; CFU, colony-forming units; PBS, phosphate buffer saline; H&E, hematoxylin-eosin; CCK-8, cell counting kit-8; NIH 3T3, NIH 3T3 mouse embryonic fibroblast cells; $FeCl_3$, ferric chloride; $CuCl_2$, cupric chloride anhydrous; FBS, fetal ovine serum; OD, optical density; BHI, brain-heart infusion broth; DMEM, dulbecco's modified eagle medium; EDTA, ethylenediaminetetraacetic acid; RBCs, red blood cells; SD, standard deviation; ANOVA, analysis of variance.

This article is part of a special issue entitled: Surface & Interface published in Materials Today Bio.

* Corresponding author.
** Corresponding author.
*** Corresponding author.
E-mail addresses: zhaoweiwei@sdu.edu.cn (W. Zhao), qizhi.zhong@ntu.edu.sg (Q.-Z. Zhong), jianhua.li@sdu.edu.cn (J. Li).

https://doi.org/10.1016/j.mtbio.2025.101525
Received 17 December 2024; Received in revised form 21 January 2025; Accepted 25 January 2025
Available online 27 January 2025

infections [12,13]. Bacterial biofilms demonstrate complex resistance mechanisms, rendering them up to 1000 times more resistant to antimicrobial agents than planktonic bacteria [14,15]. Accordingly, there is an urgent need to develop alternative therapeutic strategies to antibiotics that exhibit high antibacterial activity by disrupting these protective barriers in both bacteria and biofilm.

Ionic liquids (ILs), are a class of liquid salts with melting points at or below 100 °C, which are composed of bulky organic cations and inorganic or organic anions. The low melting point together with inherent tunable physiochemical properties endow ILs with versatile applications in a variety of areas [16]. ILs have gained significant attention in the field of antimicrobial research due to their unique physicochemical properties, including low volatility, high thermal stability, tunable solubility and tailorable antimicrobial activity [17]. Choline and geranate (CAGE), composed of choline bicarbonate and geranic acid, is classified as a third-generation of ILs with broad-spectrum antimicrobial activity against various drug-resistant bacteria, fungi, and viruses [16], including clinical isolates of *Mycobacterium tuberculosis*, *S. aureus*, and *Candida albicans*, as well as laboratory strains of *Herpes simplex virus* [18]. The antibacterial mechanisms depended on the classical micelle structure with outward cation choline bicarbonate efficiently screening the negative charge on the bacterial surface and inward lipophilic geranic acid to penetrate hydrophobic regions of the phospholipid bilayer by perturbing membrane homeostasis to lysis bacterial cells. This mechanism enables potent antimicrobial performance [19]. However, the tendency of CAGE micelles or microemulsions to aggregate and fuse can compromise the integrity of its micelle structure, reducing its chance to get in contact with bacteria and overall antibacterial efficiency. These limitations highlight the need for strategies to enhance the stability of CAGE microemulsions and bacterial adhesion ability to maximize its therapeutic potential.

Metal phenolic networks (MPNs) has emerged as a powerful platform for designing functional coatings and interfaces, integrating the mechanical and chemical properties of metal ions with the biological activities of polyphenols [20,21]. This synergy offers significant potential for applications ranging from antimicrobial coatings to advanced drug delivery systems [22]. Natural polyphenols contain numerous phenolic hydroxyl groups, which endow them with exceptional adhesive properties across a wide range of surfaces, including bacterial membranes. The adhesive properties of MPNs to bacterial cells were attributed to the phenolic groups, which can form hydrogen bonds, covalent bonds, and π-π interactions with bioactive substances on the surface of bacterial membranes [23,24]. Moreover, certain polyphenols exhibit intrinsic antimicrobial activity, making them highly versatile for biomedical applications [25,26]. In a recent study, our group reported a microencapsulation of IL by interfacial self-assembly of MPN. This approach enabled the formation of an MPN shell at the IL-water interface, effectively encapsulating the IL, improving the stability of IL droplets, and facilitating drug delivery through the gastric mucosa in a pH-responsive way [27].

In this study, we propose a strategy for preparing MPN-coated ILs microcapsules (CAGE@MPN) *via* MPN interface assembly method involving CAGE and water for antibacterial applications. The MPN shell, enriched with abundant phenolic hydroxyl groups from polyphenols, is designed to exhibit strong adhesive interactions with bacterial cells. Meanwhile, the CAGE core is anticipated to deliver potent bactericidal effects. By harnessing the dynamic adhesion properties of the MPN shell, bacteria cells are captured and adhered to the surface of the CAGE@MPN microcapsules, subsequently triggering the release of the CAGE core. The released CAGE effectively disrupts bacterial cell walls, leading to leakage of intracellular components and achieving pronounced bactericidal activity. The *in vivo* antibacterial efficiency of CAGE@MPN microcapsules was evaluated in a murine model of *S. aureus*-induced skin infection. The CAGE@MPN microcapsules effectively removes bacterial infection at wound site and promote wound healing, demonstrating significant promise for the effective treatment of bacterial infections and biofilm-associated diseases.

2. Results and discussion

2.1. Synthesis and characterization of CAGE@MPN microcapsules

Firstly, CAGE was synthesized *via* an acid-base neutralization reaction between choline bicarbonate and geranic acid with a molar ratio of 1:2, followed by removal of water and drying under reduced pressure (Fig. 1a) [18]. Then, the CAGE@MPN microcapsules were prepared using a one-pot assembly method involving ionic liquids, polyphenols, and metal ions. As illustrated in the chemical synthesis process (Fig. 1a), quercetin (Que) was initially dissolved in CAGE phase to form CAGE-Que. This CAGE-Que solution was dispersed into an aqueous medium using ultrasonic dispersion, resulting in a CAGE-Que microemulsion. Subsequently, Fe^{3+} ions were added into above CAGE-Que microemulsion, where they rapidly coordinated with Que to form MPN networks at the interface between the aqueous and ionic liquid phases. This process led to the development of a CAGE@MPN microcapsule, featuring a core-shell structure with CAGE as the core and the MPN network as the shell. The resulting CAGE@MPN microcapsules were well-dispersed in water. As shown in Fig. 1b, the brown CAGE@MPN microemulsion displayed excellent uniformity. The appearance of the characteristic ligand-to-metal charge transfer (LMCT) band at ~454 nm suggested the existence of metal-phenolic coordination (Fig. 1c) [28,29]. Fourier transform infrared spectroscopy (FTIR) analysis revealed the broading of the absorption bands at 3200-3500 cm^{-1} (corresponding to C-OH stretching band), which were originally distinct in the FTIR spectrum of CAGE@Que, suggests the formation of coordination bonds between the phenolic groups and metal ions (Fig. S1, Supporting Information). The CAGE@MPN microcapsules were characterized using a confocal laser scanning microscope (CLSM) by staining the MPN layer with BSA-FITC and loading the CAGE core with hydrophobic Nile Red (NR). As shown in Fig. 1d, intact hollow structures (MPN shell) and solid spherical structures (CAGE core) were observed in the images, confirming that the ionic liquid was successfully encapsulated within the MPN layered structure. Fig. 1e showed the fluorescence intensity distribution of the MPN shell structure and IL core. The fluorescence intensity of the MPN shell exhibited a trend of being lower in the center and higher at the edges, with the fluorescence distribution diameter slightly larger than that of the red fluorescence distribution of the IL core, further confirming the successful preparation of the CAGE@MPN microcapsules. Next, we characterized the particle morphology and stability of the microcapsules. The optical images in Fig. 1f, along with quantitative analysis of microcapsules diameter in Fig. 1g, confirm that the CAGE@MPN microcapsules were spherical in shape. After a 2-h stability test, the CAGE and CAGE-Que groups exhibited aggregation of microspheres, whereas the CAGE@MPN group maintained its original structures.

2.2. The adhesion ability of CAGE@MPN microcapsules

We hypothesized that the adhesion effect of CAGE@MPN microcapsules was due to the broad adhesion capacity of the MPN structure (Fig. 2a) [23,30,31]. The adhesion of CAGE@MPN microcapsules to *S. aureus* was investigated by quartz crystal microbalance (QCM) measurements (Fig. 2b). The sensor was typically first immersed in a *S. aureus* solution, where bacterial cells adhere to the surface, forming a bacterial biofilm. Then the sensor was exposed to CAGE and CAGE@MPN microcapsules, to evaluate their effects on bacterial adhesion. Compared with CAGE, the significant decrease in frequency (f) observed after the injection of the CAGE@MPN solution more intuitively demonstrated the enhanced binding affinity and confirmed the MPN-mediated attachment of the CAGE@MPN microcapsules on bacterial membranes (Fig. 2c). As shown in Fig. 2d, after incubating the NR-labeled CAGE@MPN microcapsules for 15 min, we observed a

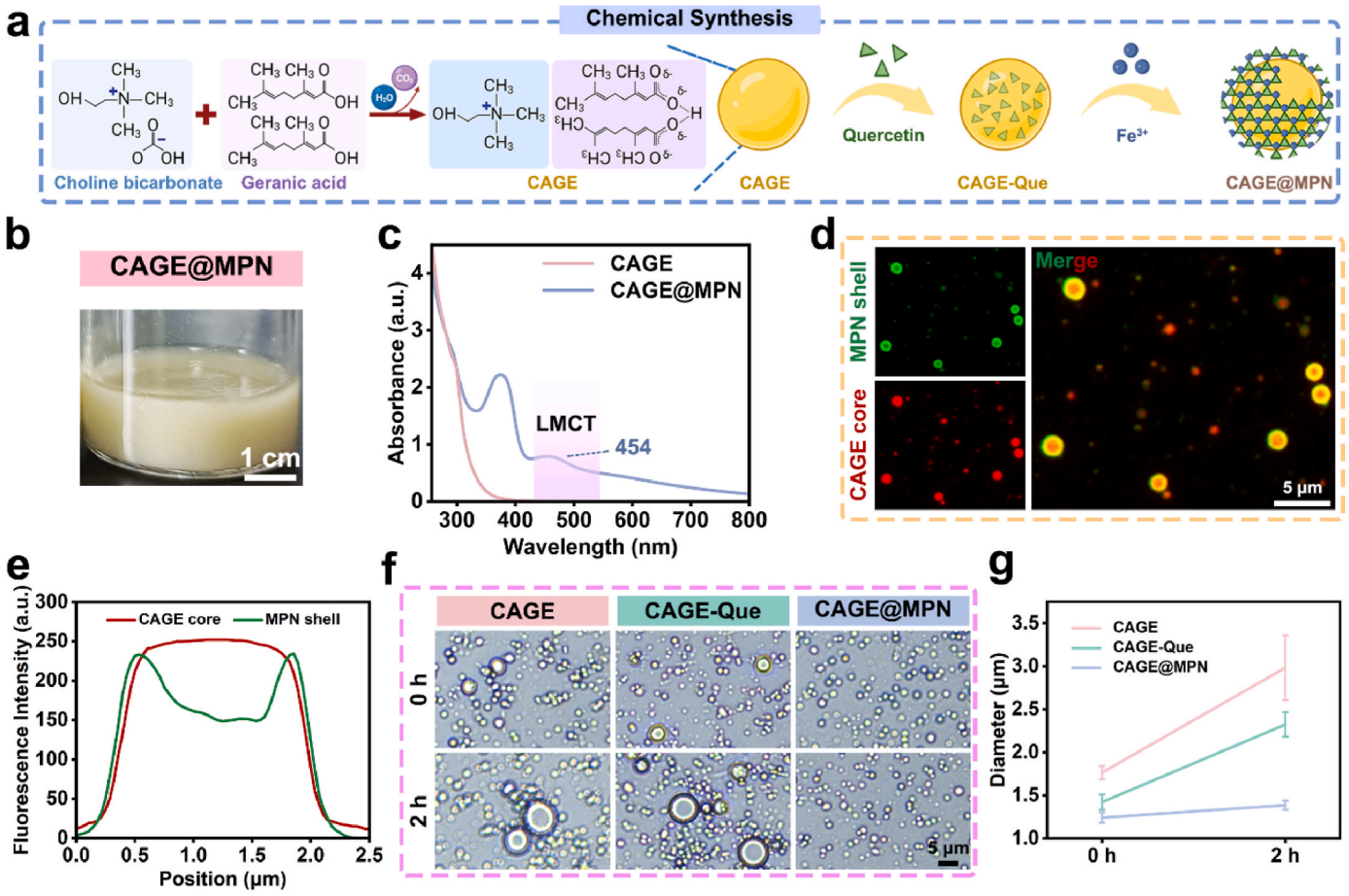

Fig. 1. Characterization of CAGE@MPN microcapsules. (a) Schematic illustration for the synthesis route of CAGE, and the preparation of CAGE@MPN microcapsules through the self-assembly of CAGE, quercetin, and Fe^{3+}. (b) Image of aqueous solutions containing CAGE@MPN microcapsules. (c) UV–vis spectrum of CAGE and CAGE@MPN microcapsules. The purple region highlights the LMCT band in the spectrum of CAGE@MPN microcapsules. (d) Fluorescence microscope images showing the core-shell structure of CAGE@MPN microcapsules. Green: MPN shell stained with BSA-FITC, Red: CAGE core stained with Nile Red. (e) Line-measurement fluorescence distribution of CAGE@MPN microcapsules. (f) Optical images and (g) quantitative results showing the stability of CAGE, CAGE-Que, and CAGE@MPN microcapsules, respectively. Data for g) presented as mean values ± standard deviations (SD) ($n = 3$ independent experiments). Error bars = SD.

strong overlap of the red fluorescence from NR on the CAGE@MPN-treated bacteria with the blue fluorescence from *S. aureus*, further supporting the previous findings. Scanning electron microscope (SEM) images in Fig. 2e showed a significant increase in the number of CAGE@MPN microcapsules on the surface of *S. aureus* cell membranes. After treated with CAGE@MPN microcapsules, the bacterial surface exhibited noticeable cavities, accompanied by the dissolution of the bacterial membrane, indicating that the CAGE@MPN microcapsules effectively disrupted the bacterial structure. We further characterized the dynamic adhesion process of CAGE@MPN microcapsules on the bacterial surface using CLSM. Fig. 2f shows the time-dependent adhesion of CAGE@MPN microcapsules to bacterial cells. Initially, CAGE@MPN microcapsules adhered to bacteria surface and, after 30 min, the microcapsules began to overlap with *S. aureus* cells, leading to a wrinkling morphology. These results suggested that within 30 min, the CAGE@MPN microcapsules effectively adhered to *S. aureus*, demonstrating their potential in bacterial adhesion targeting.

2.3. *In vitro antibacterial activity of CAGE@MPN microcapsules*

Many attempts have been contributed to combat *S. aureus* and biofilm, which provided the basis and inspiration for subsequent research [32]. Given the remarkable adhesive performances of CAGE@MPN microcapsules, we hypothesized that they would demonstrate excellent sterilization capabilities [18,33]. The antimicrobial efficacy of the CAGE@MPN microcapsules against free *S. aureus* was evaluated in this section (Fig. 3a). As shown in Fig. 3b and c, CAGE@MPN microcapsules exhibit a significantly stronger antibacterial effect compared to the Control, CAGE, and CAGE-Que groups. The bacterial morphology and internal structure were examined using SEM with the images depicted in Fig. 3d. The colony-forming units (CFU) results demonstrated that *S. aureus* in the Control group revealed intact spherical shapes with unaltered cell membranes. In contrast, the CAGE@MPN-treated *S. aureus* exhibited obvious surface wrinkles and bacterial content in the effluent, reaffirming the antibacterial effect of CAGE@MPN. Additionally, the efflux of intracellular proteins was investigated (Fig. 3e). The results revealed that protein leakage in the CAGE@MPN group was significantly higher than in the Control group, confirming that CAGE@MPN treatment leads to more pronounced bacterial structural damage and protein leakage. Meanwhile, LIVE/DEAD staining was conducted to evaluate bacterial viability (Fig. 3f). *S. aureus* in Control group exhibited intense green fluorescence, indicating a larger number of viable bacteria. In contrast, the CAGE@MPN groups exhibit intense red fluorescence, indicating that most of the bacteria had died. The above bactericidal performance can be interpreted as the broad adhesion ability of the MPNs promotes the adhesion of the CAGE@MPN microcapsules to the *S. aureus* surface, and the penetration ability of CAGE inside of the *S. aureus* bacteria to disrupt the bacterial structure.

The potential of CAGE@MPN microcapsules to eradicate mature *S. aureus* biofilms and *E. coli* biofilms was also explored. The antibiofilm

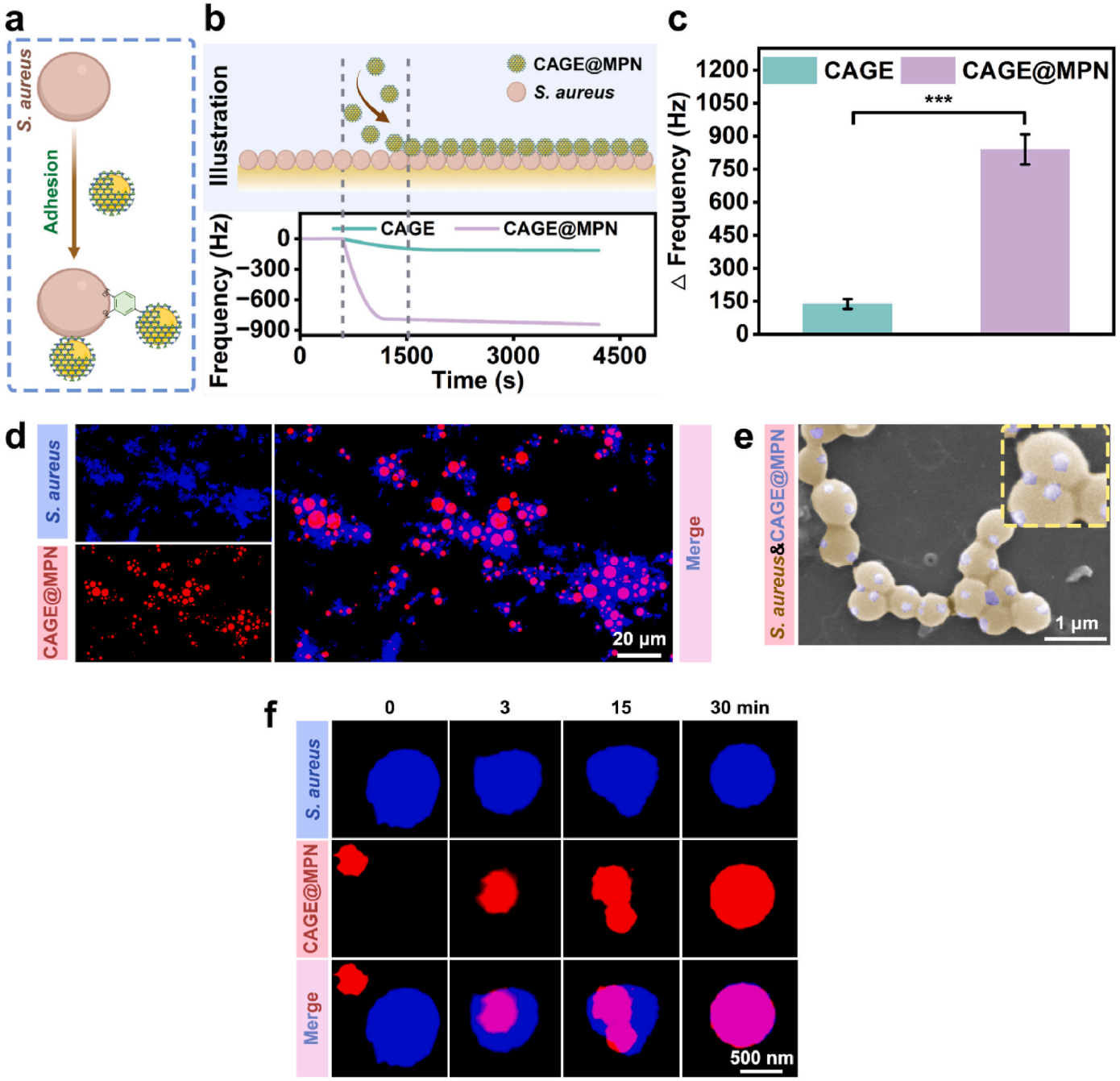

Fig. 2. The adhesive behavior of CAGE@MPN microcapsules. (a) Schematic illustration of the adhesive behavior of CAGE@MPN microcapsules to *S. aureus*. (b) Real-time QCM frequency changes during the binding of CAGE and CAGE@MPN microcapsules with *S. aureus*. (c) Quantitative results of frequency changes during the binding of CAGE and CAGE@MPN microcapsules with *S. aureus*. (d) CLSM images of adhesion performance of CAGE@MPN microcapsules to *S. aureus*. Blue: *S. aureus*, Red: CAGE@MPN microcapsules. (e) SEM images of *S. aureus* treated with CAGE@MPN microcapsules. (f) CLSM images showing the adhesion process between the CAGE@MPN microcapsules and bacteria. Blue: *S. aureus*, Red: CAGE@MPN microcapsules. Data for c) were represented as mean ± SD ($n = 3$ independent experiments). Error bars = SD. A statistically significant difference compared with the control group is indicated by $^{***}p < 0.001$.

effect of CAGE@MPN microcapsules at different concentrations was initially evaluated by measuring biofilm biomass through crystal violet staining. As shown in Fig. 3g and h, *S. aureus* biofilms remained dense and intact in absence of CAGE@MPN (0 mg mL^{-1}). However, a significant reduction in biofilm biomass was observed after the *S. aureus* biofilms were incubated with CAGE@MPN microcapsules. The OD value of the biofilm treated with CAGE@MPN (0.6 mg mL^{-1}) decreased to 25 % of that in the Control group, indicating a significant dissociation of the *S. aureus* biofilm. Furthermore, the reduction in *E. coli* biofilm biomass incubated with CAGE@MPN microcapsules have also been conducted, with only approximately 20 % of the *E. coli* biofilm remained (Fig. 3i). This further highlights the ability of CAGE@MPN microcapsules to disrupt multiple biofilm types, including both *S. aureus* and *E. coli*.

Besides, the biofilm matrix can be considered to be a shared space for the encased microbial cells, comprising a wide variety of extracellular polymeric substances (EPS), such as polysaccharides, proteins, amyloids, lipids and extracellular DNA (eDNA), as well as membrane vesicles and humic-like microbially derived refractory substances [34]. It has been reported that at CAGE had a good dissolving effect on a variety of proteins, polysaccharides and other substances [35,36]. The

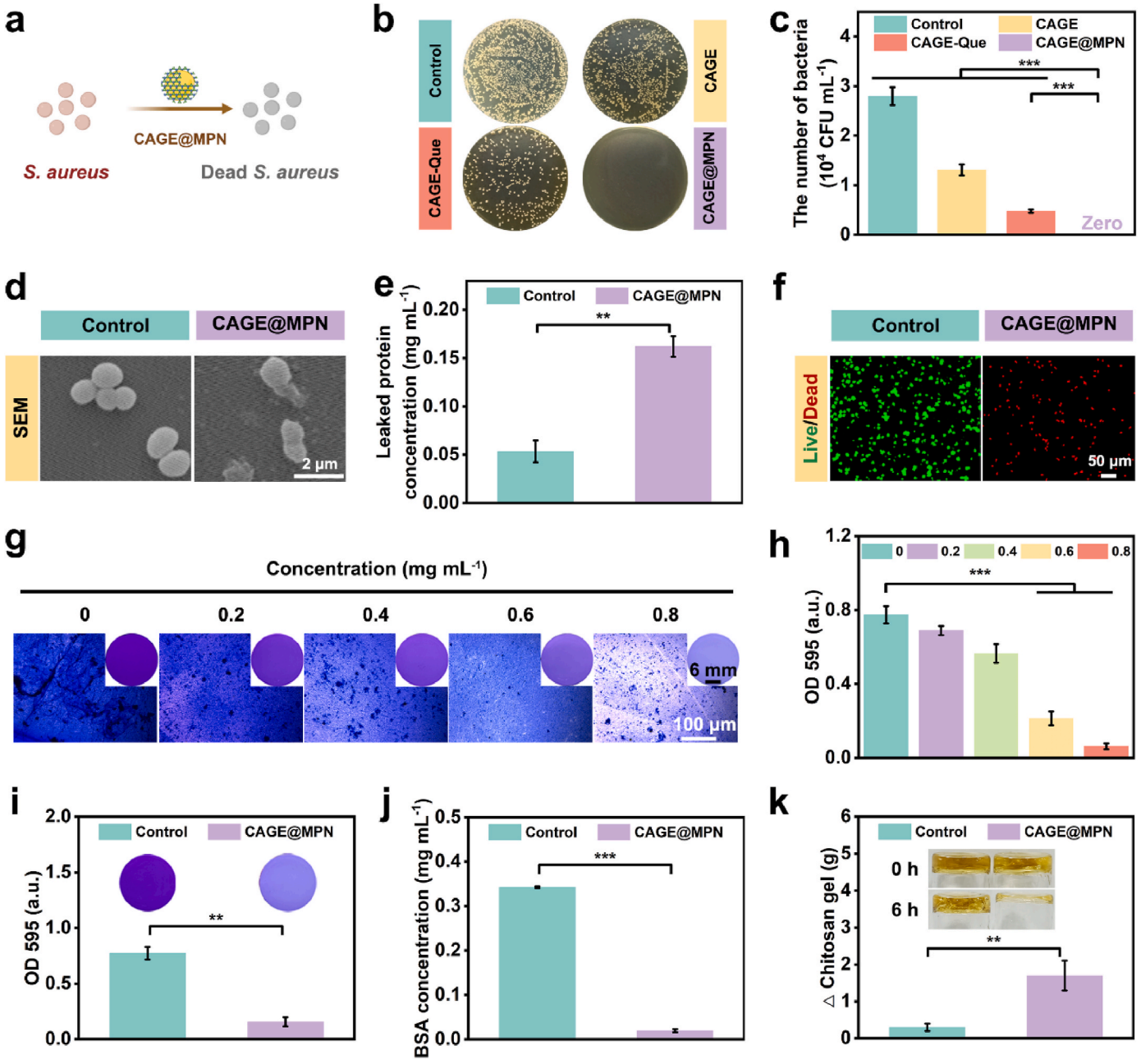

Fig. 3. Bacterial killing and biofilm removal ability of CAGE@MPN microcapsules. (a) Schematic illustration of *S. aureus* killing using CAGE@MPN microcapsules. (b) Photographs and (c) counts of *S. aureus* colonies treated with phosphate buffer saline (PBS), CAGE, CAGE-Que, and CAGE@MPN microcapsules, respectively. (d) SEM images showing *S. aureus* treated with PBS and CAGE@MPN microcapsules. (e) Measurement of leaked protein concentration in *S. aureus* treated with PBS and CAGE@MPN microcapsules. (f) LIVE/DEAD staining images of *S. aureus* incubated with PBS and CAGE@MPN microcapsules. Green: live *S. aureus*, Red: dead *S. aureus*. (g) Crystal violet staining images of *S. aureus* biofilms after treated with CAGE@MPN microcapsules. (h) Quantitative analysis of crystal violet absorbance. (i) Quantitative analysis of crystal violet absorbance and crystal violet staining images of *E. coli* biofilms after treated with CAGE@MPN. (j) Degradation of BSA after treated with CAGE@MPN. (k) Degradation of chitosan before and after treated with CAGE@MPN. Data for c, e, h, i, j, k) were represented as mean ± SD ($n = 3$ independent experiments). Error bars = SD. A statistically significant difference compared with the control group is indicated by $^{**}p < 0.01$, $^{***}p < 0.001$.

hydrophobicity anion of CAGE can dissociate from the more bulky, hydrophilic cation, and penetrate to the membrane of bacteria, allowing hydrophobic interactions with the lipid components [37]. To demonstrate the effectiveness of CAGE@MPN in degrading the biofilm EPS composition, representative biomacromolecules, specifically bovine serum albumin and chitosan, were selected as model substrates. Degradation studies of the individual components were conducted following established methodologies to mimic the degradation of EPS [38]. Protein degradation in the presence of CAGE@MPN was assessed through protein concentration measurement, and the results revealed that CAGE@MPN microcapsules induced significant degradation of protein samples (Fig. 3j). For polysaccharides, degradation studies by CAGE@MPN were performed using cross-linking chitosan gel samples, where CAGE@MPN microcapsules notably enhanced chitosan degradation, as evidenced by the loss in chitosan mass (Fig. 3k). These results suggest that CAGE@MPN are capable of efficiently breaking down bacterial biofilms by destroying biofilm matrix including polysaccharides, proteins, and lipids components. Therefore, CAGE@MPN is expected to effectively eliminate biofilms, multiple biofilms, and biofilm matrix, which is attributed to the adhesion of MPN and release of CAGE

to exert bactericidal and matrix-breaking action [39].

2.4. *In vivo* therapeutic effect of CAGE@MPN microcapsules against wound *S. aureus* infections

Based on the superior antibacterial ability of CAGE@MPN microcapsules observed *in vitro*, a murine wound infection model was established by inoculating *S. aureus* onto the superficial wound to investigate the *in vivo* antibacterial potential of CAGE@MPN microcapsules. Previous studies have demonstrated that the incorporation of metal ions played a crucial role in antibacterial and wound healing performances [40,41]. Given the high modularity of MPNs, two metal ions, Fe^{3+} and Cu^{2+}, were selected for separate incorporation into the synthesis of CAGE@MPN microspheres to evaluate their antibacterial effects *in vivo*. The *S. aureus*-infected mice were randomly divided into three groups: Control, CAGE@MPN-Fe, and CAGE@MPN-Cu. Each group was treated with different formulations *via* local administration respectively (Fig. 4a). The wounds were photographed and measured daily to compare the therapeutic efficacy among different groups (Fig. 4b and c). The biofilm in the CAGE@MPN microcapsules treated groups eliminated significantly by the 4th day, while the Control group still exhibited persistent gray-white biofilm in the skin wounds. After ten days of treatment, both the CAGE@MPN-Fe treated and CAGE@MPN-Cu treated groups exhibited favorable therapeutic outcomes. It was demonstrated that the CAGE@MPN-Cu treatment group achieved rapid wound healing due to the excellent antibacterial properties of CAGE@MPN microcapsules and the enhanced tissue healing capabilities of Cu^{2+} [42–44]. However, significant scabs were still observed in the Control group. The residual *S. aureus* in wound tissues was measured using a standard plate count method on the 4th day. As indicated in Fig. 4d, the CAGE@MPN-Fe, and CAGE@MPN-Cu groups demonstrated substantial antibacterial effect, with a reduction of over 95 % in the *S. aureus* population. Furthermore, Fig. 4e illustrated a consistent increase in body weight across all three groups, indicating the safety of all samples in mice.

Hematoxylin-Eosin (H&E) staining images (Fig. 5a) revealed a substantial increase in newly formed epidermis (Fig. 5b) and a noticeable reduction in neutrophils (Fig. 5c) in the two CAGE@MPN groups, while the Control group displayed a less favorable healing state. Proper collagen deposition is essential for improving tensile strength during the

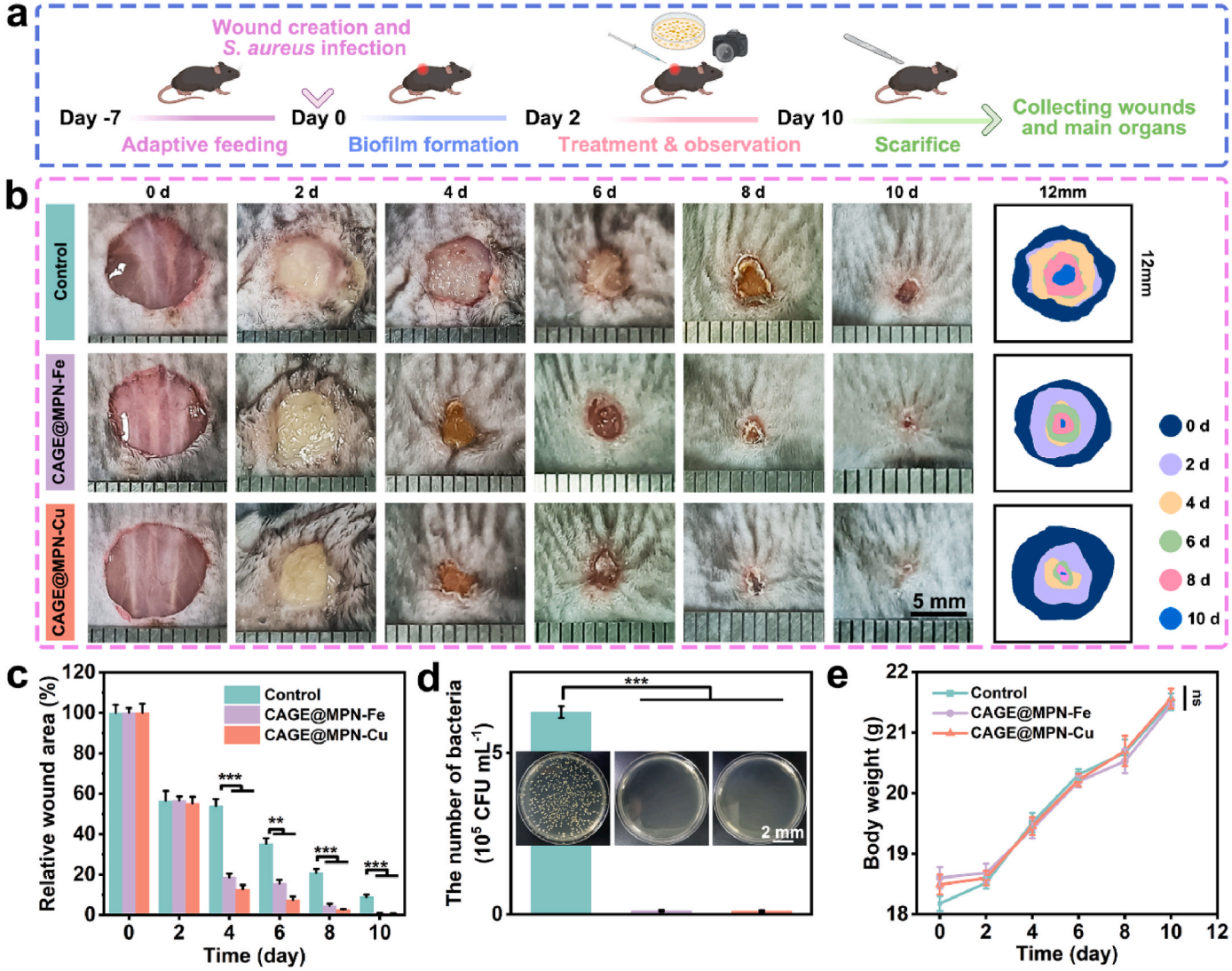

Fig. 4. The *in vivo* antimicrobial ability of CAGE@MPN microcapsules on a *S. aureus*-induced wound infection model in mice. (a) The scheme illustrated the construction of the murine skin bacterial infection model and the treatment protocol with different formulations. (b) Photos of mice wounds after different treatments in 10 days. (c) Statistical results of wound areas after different treatments. (d) *S. aureus* colony counting and photos of wound tissue after different treatments on the day 4. (e) Body weight changes of *S. aureus*-infected mice after different treatments. Data for c, d, e) were represented as mean ± SD ($n = 4$ independent experiments). Error bars = SD. A statistically significant difference compared with the control group is indicated by $^{**}p < 0.01$; $^{***}p < 0.001$; *ns, no significance.*

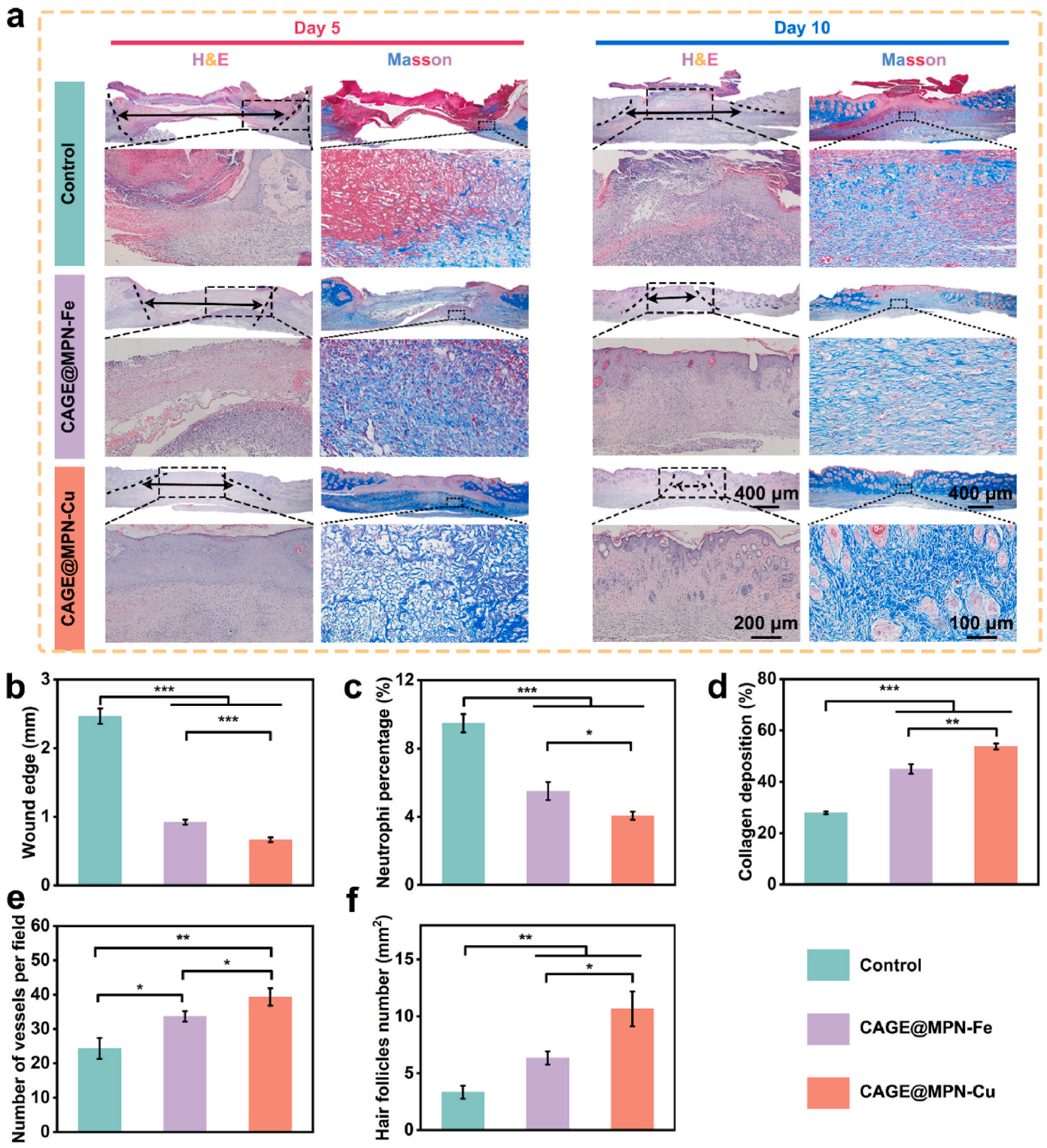

Fig. 5. *In vivo* histopathological analysis of wounds treated with various samples. (a) H&E and Masson staining images of the wound issues in each group on day 5 and day 10. (b) Wound edge, (c) neutrophils percentage, (d) collagen volume fraction, (e) number of vessels, and (f) hair follicles number in wounds with diverse treatments at day 10. Data for b, c, d, e, f) were represented as mean ± SD ($n = 4$ independent experiments). Error bars = SD. A statistically significant difference compared with the control group is indicated by $^{*}p < 0.05$, $^{**}p < 0.01$, $^{***}p < 0.001$.

remodeling process. And collagen fibers provide a scaffold for the attachment and migration of immune cells and epithelial cells within the tissue microenvironment, thereby promoting wound epithelialization and the construction of vascular network [45]. Therefore, Masson's trichrome staining was performed at the wound sites to identify newly formed collagen fibers. Fig. 5d shows clear and compact collagen fibers present in the both CAGE@MPN groups, demonstrating dense deposition of collagen fibers, further supporting their role in facilitating effective wound healing. The statistical analysis of wound edge, neutrophil percentage, and collagen deposition reveals that the CAGE@MPN-Cu group significantly outperforms the CAGE@MPN-Fe group, accompanied by more angiogenesis and hair follicle formation

(Fig. 5e and f). This is attributed to the fact that Cu^{2+} plays an important role in angiogenesis by stimulating the proliferation and migration of endothelial cells, as well as inducing the expression of vascular endothelial growth factor (VEGF), thereby accelerating neovascularization [46]. Therefore, CAGE@MPN-Cu exhibits a superior ability to promote infected wound healing by clearing biofilms and facilitating angiogenesis, ultimately achieving tissue regeneration.

2.5. Biocompatibility assessment

The excellent biocompatibility of CAGE@MPN microcapsules is essential for their biomedical applications *in vivo*. As illustrated in Fig. 6a, the cytotoxicity of CAGE@MPN microcapsules was evaluated using the cell counting kit-8 (CCK-8) assay on NIH 3T3 mouse embryonic fibroblast cells (NIH 3T3), a hemolysis test on red blood cells, LIVE/DEAD staining assay of NIH 3T3 cells, and H&E staining of major organs. As shown in Fig. 6b, CAGE@MPN microcapsules maintained high cell viability of NIH 3T3 cells (>95 %) in the concentrations range of 0.2–0.8 mg mL^{-1}, indicating favorable biocompatibility at the cellular level. Fig. 6c demonstrated that the hemolysis rates below 5 % for all samples, meeting the threshold for hemocompatibility. LIVE/DEAD staining results (Fig. 6d) revealed green fluorescence and intact morphology in NIH 3T3 cells across all groups, with no observable differences compared to the Control group, further confirming their cytocompatibility. Moreover, histological analysis of major organs, including the heart, liver, spleen, lung, and kidney, performed after 10 days of treatment revealed no noticeable damages or inflammatory lesions (Fig. 6e), underscoring the *in vivo* safety of CAGE@MPN microcapsules. These findings collectively highlight the potential of CAGE@MPN microcapsules for safe and effective biomedical applications.

3. Conclusions

In summary, CAGE@MPN microcapsules were successfully synthesized through the interfacial coordination interactions between metal ions and polyphenols at the interface of ionic liquid and water. The phenolic hydroxyl groups in natural polyphenols imparted the MPN shell with extensive adhesive capabilities, enabling effective adherence to bacterial surfaces. The CAGE@MPN disrupted the structure of the bacterial cell wall, resulting in leakage of intracellular contents and demonstrating potent bactericidal activity. The *in vitro* adhesive effect of CAGE@MPN microcapsules to bacteria were confirmed by SEM, CLSM, and QCM assays. The bactericidal and anti-biofilm effects of MPN and CAGE in CAGE@MPN microcapsules were confirmed through colony-counting assay, SEM, intracellular protein leakage, live/dead staining, and crystal violet staining assays. Additionally, CAGE@MPN microcapsules exhibited minimal cytotoxicity and hemolysis *in vitro*. In a mouse model of *S. aureus* skin infection, CAGE@MPN microcapsules exhibited significant bacterial clearance and wound healing effects, highlighting their potential for treating *S. aureus* infections. This research demonstrated the excellent therapeutic efficacy in managing bacterial infections *in vivo*, offering a promising strategy for the treatment of bacterial infections in the future.

4. Experimental section

Material: Choline bicarbonate was obtained from Sigma-Aldrich (USA). Geranic acid was purchased from Thermo Fisher Scientific (USA). Quercetin and Nile Red was obtained from Shanghai Macklin Biochemical Technology Co., Ltd. (China). Ferric chloride ($FeCl_3$) and Cupric Chloride Anhydrous ($CuCl_2$) were obtained from Adamas-beta (China). Calcein/PI Cell Viability/Cytotoxicity Assay Kit (C2015M) was purchased from Beyotime Biotechnology (China). CCK-8 (521942) was purchased from Biosharp (China). Mannose-PEG-SH (2,000) was purchased from MeloPEG Tech.Inc. (Shanghai, China). PBS and fetal bovine serum (FBS) (04-001-1ACS) were purchased from BIOIND. All reagents used were of analytical grade. Triple distilled water was used throughout the experiments.

Preparation of CAGE@MPN microcapsules: CAGE was synthesized from Choline bicarbonate and geranic acid. Choline bicarbonate was slowly added to geranic acid at a molar ratio of 1:2. The mixture was stirred at 40 °C until CO_2 evolution ceased. Residual water was removed by rotary evaporation at 60 °C for 2 h followed by drying in a vacuum oven for 48 h at 60 °C. Quercetin was dissolved in aqueous solution of CAGE (1 mg mL^{-1}) under the action of magnetic stirring. 200 mg CAGE-Que (1 mg mL^{-1}) was added in to 3.6 mL triple distilled water with an ultrasonic treatment using a needle probe sonicator (JY96-IIN, Scientz, Ningbo, China) at 40 % amplitude (260W) for 1 min. 8 μL $FeCl_3{\cdot}6H_2O$ (8 mg mL^{-1}) was immediately added to the above mixture. Then, 100 μL 0.1 M NaOH aqueous solution was added to adjust the final pH to ~8.0.

Characterization of CAGE@MPN microcapsules: The CAGE@MPN microcapsules were characterized by confocal laser scanning microscopy (CLSM, Carl Zeiss LSM780, Germany). CAGE phase was stained with Nile Red (red) before the MPN shell formation, and the MPN layer was fluorescently labeled with BSA-FITC (green) after microcapsules formation. UV–vis absorption spectra were acquired using a UV–vis spectrophotometer (UV-2600i, Shimadzu, Japan).

SEM: CAGE@MPN were added to an equal volume of bacterial solution (500 μL, 1×10^8 CFU mL^{-1}) to 2-mL centrifuge tubes, and then incubated at 37 °C for 30 min. Next, the samples were fixed with 4 % paraformaldehyde for 1 h. They were then dehydrated using a graded ethanol series (30 %, 50 %, 70 %, 90 %, and 100 % ethanol). The dehydrated bacteria were fixed on a silicon wafer. The silicon wafer was subsequently sputter-coated with gold for SEM observation.

Confocal laser scanning microscopy observation: The *S. aureus* cells (2×10^8 CFU mL^{-1}, 50 μL) were stained by Hoechst 33342, mixed with equal volume of CAGE@MPN (0.8 mg mL^{-1}) and cultured for 15 min. The bacterial suspension was immobilized onto a microscope slide and observed by CLSM (Olympus, FV3000).

Bacterial affinity assay: The quartz crystal microbalance (QCM) was used to test the binding force between CAGE@MPN and bacterial. The preparation procedure of the QCM chip was as follows: the chip (Au) was immersed in 2 mL of Mannose-PEG-SH solution (2 mg mL^{-1}) for 12 h and washed with PBS, followed by immersion in 2 mL of bacterial suspension (1×10^8 CFU mL^{-1}) for another 12 h. Finally, the unspecifically bound bacterial was washed away with PBS and the chip was dried for use. All tests were performed on a QSense Analyzer using a peristaltic pump (30 μL min^{-1}) in circulation mode. Finally, we assessed the strength of the CAGE@MPN-bacterial binding force by the magnitude of the frequency change.

In vitro antibacterial activity of CAGE@MPN microcapsules: To determine the antibacterial properties of CAGE@MPN microcapsules against *S. aureus*. CAGE, CAGE-Que, and CAGE@MPN were added to an equal volume of bacterial solution (500 μL, 1×10^8 CFU mL^{-1}) to 2-mL centrifuge tubes, and then incubated at 37 °C for 30 min. Subsequently, the bacterial samples were diluted in PBS (1×10^4 folds), and 100 μL of the diluted bacterial suspension was spread on solid Brain-heart infusion broth (BHI) plates. Finally, the CFUs were counted after incubation for 20 h at 37 °C, according to the counted CFUs, and the antibacterial ratio was calculated.

LIVE/DEAD bacterial assay: To examine the viability of bacteria after CAGE@MPN treatment, after incubation with CAGE@MPN microcapsules for 30 min, *S. aureus* was centrifuged and stained with NucGreen (green)/PI (red) using LIVE/DEAD bacterial viability kits in the dark for 25 min and then imaged by CLSM (Olympus, FV3000).

Bacterial protein leakage measurement: 1×10^8 CFU mL^{-1} of *S. aureus* were incubated with CAGE@MPN microcapsules and incubated at 37 °C for 30 min. The solution was then centrifuged at 10000 rpm for 5 min at 4 °C. The supernatant liquid was transferred to a 96-well plate and the protein leakage concentrations were measured by the Bradford Protein Assay Kit on a microplate reader and read at 595

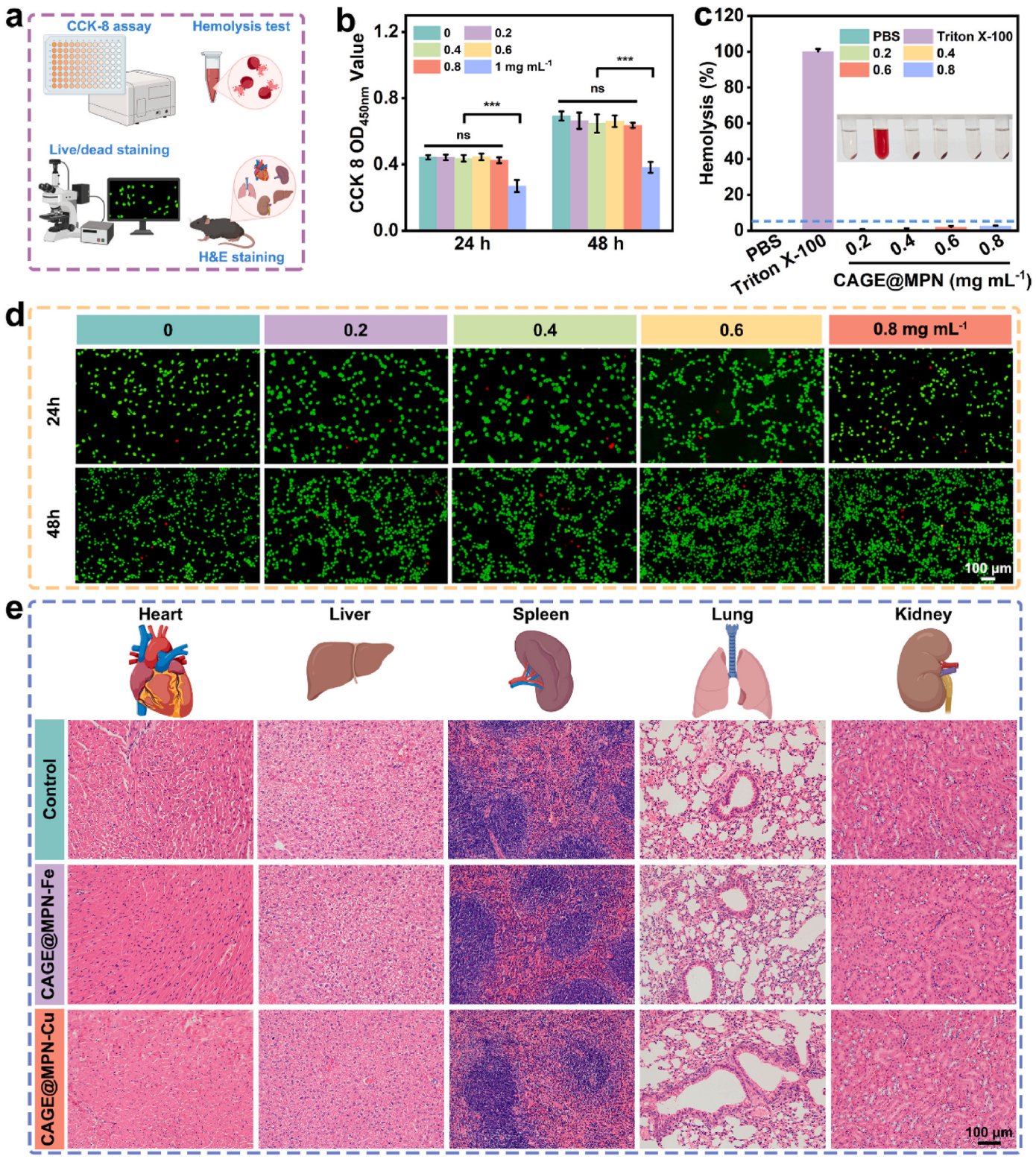

Fig. 6. The biocompatibility of the CAGE@MPN microcapsules. (a) The scheme illustrated the methods for biocompatibility testing. (b) CCK-8 assay of NIH 3T3 cells treated with diverse samples. (c) Hemolysis assay of different samples incubated with fresh blood samples. Insets are corresponding images of supernatant in hemolysis experiment. (d) LIVE/DEAD staining of NIH 3T3 cells with diverse treatments. (e) H&E staining images of major organs (heart, liver, spleen, lung, kidney) after different treatments on day 10 in *S. aureus*-infected mice. Data for b, c) were represented as mean ± SD ($n = 3$ independent experiments). Error bars = SD. A statistically significant difference compared with the control group is indicated by $***p < 0.001$; *ns, no significance*.

nm.

Crystal violet staining of bacterial biofilm: When the biofilm formed, the samples were replaced with medium containing CAGE@MPN or PBS, and then they were cultured at 37 °C for 24 h. After treatments, glutaraldehyde solution (2.5 %, 200 μL) was added into each well to fix the biofilm for 30 min. Next, the biofilms were stained by crystal violet solution (0.1 %, 200 μL) for 20 min. Eventually, the stained biofilms were rinsed with PBS and then naturally air-dried. The crystal violet staining images were acquired by scanner (EPSON, Japan). In order to quantitatively measure residual biofilm content, ethanol solution (95 %, 200 μL) was added into each well to rinse the dyed biofilm. The optical density (OD) value of each sample was tested at 595 nm.

Cleavage of proteins: Protein cleavage assays were performed at 37 °C for 6 h in 80 μL CAGE@MPN microcapsules containing 1 mg mL^{-1} BSA by Bradford Protein Assay Kit.

Cleavage of Polysaccharides: Chitosan was chosen as a model polysaccharide, and chitosan hydrogel was prepared with glutaraldehyde cross-linking. Chitosan (0.5 %) was dissolved in 2 mL HAc-NaAc (0.1 M, pH 4.5) and incubated with 1 % glutaraldehyde at 37 °C. The formed hydrogel appeared yellow in glass vials and its mass was recorded. Next, 1 mL CAGE@MPN (0.8 mg mL^{-1}) was added to cover the gel in the glass vial prior to sample incubation at 37 °C for 6 h. The supernatant was then discarded and the remaining gel was rinsed 3 times with water. Inversion to filter paper for 1 h was performed to remove water and un-crosslinked chitosan, and the mass of the remaining gel was recorded. The volume of gel remaining in the glass vial was visualized after inversion and the mass difference was recorded.

Cell culture: Mouse embryonic fibroblast (NIH 3T3) cells were cultured in a Dulbecco's modified eagle medium (DMEM) medium (high glucose) containing 10 % FBS, and 1 % penicillin-streptomycin solution in a humidified atmosphere incubator with 37 °C, 95 % air and 5 % carbon dioxide.

Cytocompatibility evaluation in vitro: NIH 3T3 cells were seeded in 96-well plates with the density of 1×10^5 cells per well, respectively, followed by incubation for 12 h. CAGE@MPN microcapsules were suspended in a culture medium with concentrations of 0, 0.2, 0.4, 0.6, 0.8, and 1.0 mg mL^{-1} and incubated with NIH 3T3 cells for 24 and 48 h. CCK-8 was conducted to evaluate the cell cytocompatibility of CAGE@MPN microcapsules following the manufacturer's protocol. Option density at 450 nm was measured using a microplate reader (SPECTROstar Nano, BMG LABTECH) to quantify cell viability. LIVE/DEAD viability was also employed to evaluate the cell status of NIH 3T3 cells following its instructions. The fluorescence-stained cells were observed with the epi-fluorescence microscope (BX-53, Olympus).

Hemolysis Assays: Fresh blood samples from mice were collected into tubes containing ethylenediaminetetraacetic acid (EDTA), which were centrifuged immediately (within 30 min of collection) (RCF, 3000 g, 10 min, 4 °C) to remove serum. Fresh red blood cells (RBCs) were then washed thrice with PBS. Following the last wash, the RBCs were diluted with sterile isotonic PBS to obtain an RBC stock suspension (4 vol% blood cells). The RBC stock suspension (200 μL) was added to 1.5 mL CAGE@MPN solutions. After incubation at 37 °C for 1 h, the mixtures were centrifuged separately at RCF of 1000 g for 10 min. The hemoglobin absorption at 576 nm (OD576 sample) of each supernatant (150 μL) was recorded separately. Hemolysis activity was then determined according to the following formula:

$$\text{Hemolysis (\%)} = [(OD576_{\text{sample}} - OD576_{\text{blank}}) / (OD576_{\text{Triton}} - OD576_{\text{blank}})] \quad (1)$$

In vivo treatment of S. aureus-infected wound by CAGE@MPN microcapsules: Animal experiments were approved by the Ethics Committee of the School of Stomatology, Shandong University (NO.20231108). C57 mice (6 weeks, male) were used and purchased from Beijing Vital River Laboratory Animal Technology Co., Ltd. After anesthetizing the mice with isoflurane, dorsal hair was shaved by a razor, and the exposed area was disinfected with iodine. Circular wounds (8 mm in diameter) were created on the back of each mouse using a surgical scalpel. To establish infected wound models, each wound was infected with 50 μL *S. aureus* (1×10^8 CFU mL^{-1}). A transparent dressing was applied on the defected skin surface to protect the wound from the interference of the external environment. Following 48 h of biofilm formation post-infection, the mice were divided randomly into 3 groups: Control, CAGE@MPN-Fe, and CAGE@MPN-Cu. 100 μL of 0.8 mg mL^{-1} CAGE@MPN-Fe and CAGE@MPN-Cu were injected *in situ* into defects using pipetting tips, and 100 μL PBS was injected *in situ* into the defects of Control groups. The treatments were performed on day 2, 4, 6, 8 and the wounds were photographed. Defects and major organs were collected for area changing, bacterial counting, and H&E staining according to the schedule.

Statistics Analysis: All values were reported as the mean ± the standard deviation (SD). Comparisons of three or more groups were compared by assessing one-way or two-way analysis of variance (ANOVA) with Tukey's HSD post hoc test using GraphPad Prism software (MacKiev Software, U.S.A.). P value < 0.05 was considered statistically significant.

CRediT authorship contribution statement

Ying Wang: Writing – original draft, Software, Methodology, Investigation, Formal analysis, Data curation. **Zhibang Li:** Writing – original draft, Methodology, Investigation, Formal analysis. **Lingli Ji:** Methodology, Investigation, Formal analysis. **Jiao Sun:** Methodology, Investigation, Formal analysis. **Fei Gao:** Methodology, Investigation, Formal analysis. **Ruiqing Yu:** Software, Methodology, Investigation. **Kai Li:** Software, Methodology, Investigation. **Wenjun Wang:** Software, Project administration, Methodology, Investigation. **Weiwei Zhao:** Writing – review & editing, Visualization, Validation, Supervision, Methodology, Investigation, Funding acquisition, Conceptualization. **Qi-Zhi Zhong:** Writing – review & editing, Visualization, Validation, Supervision, Methodology, Investigation, Conceptualization. **Shaohua Ge:** Writing – review & editing, Visualization, Validation, Supervision, Investigation, Funding acquisition. **Jianhua Li:** Writing – review & editing, Visualization, Validation, Supervision, Project administration, Methodology, Investigation, Funding acquisition, Conceptualization.

Declaration of competing interest

The authors declare that they have no known competing financial interests or personal relationships that could have appeared to influence the work reported in this paper.

Acknowledgements

This work was supported by the National Natural Science Foundation of China (82470981, 82101042, 52100191, 82320108004, 82301081), National Key Research and Development Program of China (2023YFC250630), the Taishan Scholars Program of Shandong Province (tsqn201909180, tsqn202312344), Shandong Province Key Research and Development Program (2024CXPT090, 2021ZDSYS18 and 2022CXGC020511), Shandong Province Major Scientific and Technical Innovation Project (No.2021SFGC0502), the Independent Training and Innovation Team in Jinan (No. 202228055), Natural Science Foundation of Shandong Province (CN) (ZR2022QB103), Open Foundation of State Key Laboratory of Oral Diseases (SKLOD2024OF07) and Qilu Young Scholar Foundation of Shandong University, Young Scholars Program of Shandong University. We thank Translational Medicine Core Facility of Shandong University for consultation and instrument availability that supported this work.

Appendix A. Supplementary data

Supplementary data to this article can be found online at https://doi.org/10.1016/j.mtbio.2025.101525.

Data availability

Data will be made available on request.

References

[1] C.J.L. Murray, K.S. Ikuta, F. Sharara, L. Swetschinski, G. Robles Aguilar, A. Gray, et al., Global burden of bacterial antimicrobial resistance in 2019: a systematic analysis, Lancet 399 (10325) (2022) 629–655.

[2] A. Wang, L. Li, L. Zheng, B.-P. Jiang, Y. Liu, R. Huang, et al., A universal gelation strategy of bivalent anions to construct nanofibrous lysozyme hydrogels for immunomemory anti-recurrence of diabetic wound infection by activating the cGAS-STING pathway, Aggregate (2024) e662.

[3] R. Laxminarayan, The overlooked pandemic of antimicrobial resistance, Lancet 399 (10325) (2022) 606–607.

[4] L. Han, Z. Yuan, H.-M. Ren, W. Song, R. Wu, J. Li, et al., Infection-responsive polysaccharide-based drug-loaded nano-assembly for dual-modal treatment against drug-resistant bacterial lung infection, BME Mat 2 (3) (2024) e12082.

[5] J.L. Seidelman, C.R. Mantyh, D.J. Anderson, Surgical site infection prevention: a review, JAMA 329 (3) (2023) 244–252.

[6] W.R. Miller, C.A. Arias, ESKAPE pathogens: antimicrobial resistance, epidemiology, clinical impact and therapeutics, Nat. Rev. Microbiol. 22 (10) (2024) 598–616.

[7] P.P. Kalelkar, M. Riddick, A.J. García, Biomaterial-based antimicrobial therapies for the treatment of bacterial infections, Nat. Rev. Mater. 7 (1) (2022) 39–54.

[8] S. Wang, W.-Y. Wu, J.C.C. Yeo, X.Y.D. Soo, W. Thitsartarn, S. Liu, et al., Responsive hydrogel dressings for intelligent wound management, BME Mat 1 (2) (2023) e12021.

[9] J. Zhang, H. Guo, M. Liu, K. Tang, S. Li, Q. Fang, et al., Recent design strategies for boosting chemodynamic therapy of bacterial infections, Exploration 4 (2) (2024) 20230087.

[10] X. Chen, D. Missiakas, Novel antibody-based protection/therapeutics in *Staphylococcus aureus*, Annu. Rev. Microbiol. 78 (2024) 425–446.

[11] M. Rausch, J.P. Deisinger, H. Ulm, A. Müller, W. Li, P. Hardt, et al., Coordination of capsule assembly and cell wall biosynthesis in *Staphylococcus aureus*, Nat. Commun. 10 (1) (2019) 1404.

[12] E.A. Masters, B.F. Ricciardi, K.L.d.M. Bentley, T.F. Moriarty, E.M. Schwarz, G. Muthukrishnan, Skeletal infections: microbial pathogenesis, immunity and clinical management, Nat. Rev. Microbiol. 20 (7) (2022) 385–400.

[13] L. Li, Y. Yin, S. Zhang, J. Yang, P. Li, H. Zhou, et al., Triggerable Biomaterials-Based Osteomyelitis Theranostics, BME Mat, 2024 e12081.

[14] M. Yang, J. Zhang, Y. Wei, J. Zhang, C. Tao, Recent advances in metal-organic framework-based materials for anti-*Staphylococcus aureus* infection, Nano Res. 15 (7) (2022) 6220–6242.

[15] C. Wang, S. Lv, Z. Sun, M. Xiao, H. Fu, L. Tian, et al., A self-regulated phototheranostic nanosystem with single wavelength-triggered energy switching and oxygen supply for multimodal synergistic therapy of bacterial biofilm infections, Aggregate 5 (5) (2024) e587.

[16] Y. Hu, Y. Xing, H. Yue, T. Chen, Y. Diao, W. Wei, et al., Ionic liquids revolutionizing biomedicine: recent advances and emerging opportunities, Chem. Soc. Rev. 52 (20) (2023) 7262–7293.

[17] N. Nikfarjam, M. Ghomi, T. Agarwal, M. Hassanpour, E. Sharifi, D. Khorsandi, et al., Antimicrobial ionic liquid-based materials for biomedical applications, Adv. Funct. Mater. 31 (42) (2021) 2104148.

[18] M. Zakrewsky, A. Banerjee, S. Apte, T.L. Kern, M.R. Jones, R.E.D. Sesto, et al., Choline and geranate deep eutectic solvent as a broad-spectrum antiseptic agent for preventive and therapeutic applications, Adv. Healthcare Mater. 5 (11) (2016) 1282–1289.

[19] E.E.L. Tanner, K.M. Piston, H. Ma, K.N. Ibsen, S. Nangia, S. Mitragotri, The influence of water on choline-based ionic liquids, ACS Biomater. Sci. Eng. 5 (7) (2019) 3645–3653.

[20] H. Ejima, J.J. Richardson, K. Liang, J.P. Best, M.P. van Koeverden, G.K. Such, et al., One-step assembly of coordination complexes for versatile film and particle engineering, Science 341 (6142) (2013) 154–157.

[21] Y. Zhao, Y. Shi, H. Yang, M. Liu, L. Shen, S. Zhang, et al., Stem cell microencapsulation maintains stemness in inflammatory microenvironment, Int. J, Oral Sci. 14 (1) (2022) 48.

[22] Y. Wang, Z. Li, R. Yu, Y. Chen, D. Wang, W. Zhao, et al., Metal-phenolic network biointerface-mediated cell regulation for bone tissue regeneration, Mater. Today Bio 30 (2025) 101400.

[23] F. Centurion, S. Merhebi, M. Baharfar, R. Abbasi, C. Zhang, M. Mousavi, et al., Cell-mediated biointerfacial phenolic assembly for probiotic nano encapsulation, Adv. Funct. Mater. 32 (26) (2022) 2200775.

[24] J. Liu, W. Li, Y. Wang, Y. Ding, A. Lee, Q. Hu, Biomaterials coating for on-demand bacteria delivery: selective release, adhesion, and detachment, Nano Today 41 (2021) 101291.

[25] Z. Li, Z. Chen, H. Chen, K. Chen, W. Tao, X.-k. Ouyang, et al., Polyphenol-based hydrogels: pyramid evolution from crosslinked structures to biomedical applications and the reverse design, Bioact. Mater. 17 (2022) 49–70.

[26] Y. Fan, L. Zheng, M. Jin, X. Li, Z.A. Li, X. Wang, Mussel-mimetic polysaccharide-based injectable hydrogels for biomedical applications, BME Mat (2024) e12089.

[27] L. Shen, Y. Zhang, J. Feng, W. Xu, Y. Chen, K. Li, et al., Microencapsulation of ionic liquid by interfacial self-assembly of metal-phenolic network for efficient gastric absorption of oral drug delivery, ACS Appl. Mater. Interfaces 14 (40) (2022) 45229–45239.

[28] W. Xu, S. Pan, B.B. Noble, J. Chen, Z. Lin, Y. Han, et al., Site-selective coordination assembly of dynamic metal-phenolic networks, Angew. Chem. Int. Ed. 61 (34) (2022) e202208037.

[29] O. Mazaheri, Z. Lin, W. Xu, M. Mohankumar, T. Wang, A. Zavabeti, et al., Assembly of silicate–phenolic network coatings with tunable properties for controlled release of small molecules, Adv. Mater. (2024) 2413349.

[30] H. Luo, F. Wu, X. Wang, S. Lin, M. Zhang, Z. Cao, et al., Encoding bacterial colonization and therapeutic modality by wrapping with an adhesive drug-loadable nanocoating, Mater. Today 62 (2023) 98–110.

[31] P. Liu, Y. Wu, B. Mehrjou, K. Tang, G. Wang, P.K. Chu, Versatile phenol-incorporated nanoframes for *in situ* antibacterial activity based on oxidative and physical damages, Adv. Funct. Mater. 32 (17) (2022) 2110635.

[32] A. Tiwari, P. Sharma, B. Vishwamitra, G. Singh, Review on surface treatment for implant infection *via* gentamicin and antibiotic releasing coatings, Coatings 11 (8) (2021) 1006.

[33] K.N. Ibsen, H. Ma, A. Banerjee, E.E.L. Tanner, S. Nangia, S. Mitragotri, Mechanism of antibacterial activity of choline-based ionic liquids (CAGE), ACS Biomater. Sci. Eng. 4 (7) (2018) 2370–2379.

[34] H.-C. Flemming, E.D. van Hullebusch, T.R. Neu, P.H. Nielsen, T. Seviour, P. Stoodley, et al., The biofilm matrix: multitasking in a shared space, Nat. Rev. Microbiol. 21 (2) (2023) 70–86.

[35] A. Banerjee, K. Ibsen, Y. Iwao, M. Zakrewsky, S. Mitragotri, Transdermal protein delivery using choline and geranate (CAGE) deep eutectic solvent, Adv. Healthcare Mater. 6 (15) (2017) 1601411.

[36] Q.M. Qi, S. Mitragotri, Mechanistic study of transdermal delivery of macromolecules assisted by ionic liquids, J. Control. Release 311–312 (2019) 162–169.

[37] H. Albadawi, Z. Zhang, I. Altun, J. Hu, L. Jamal, K.N. Ibsen, et al., Percutaneous liquid ablation agent for tumor treatment and drug delivery, Sci. Transl. Med. 13 (580) (2021) eabe3889.

[38] L. Wang, Y. Miao, M. Lu, Z. Shan, S. Lu, J. Hou, et al., Chloride-accelerated Cu-Fenton chemistry for biofilm removal, Chem. Commun. 53 (43) (2017) 5862–5865.

[39] S. Mitragotri, Choline geranate (CAGE): a multifaceted ionic liquid for drug delivery, J. Control. Release 376 (2024) 593–600.

[40] P. Sharma, S. Rohila, U. Hasan, P.H. Krishna, C. Ugwuegbu, A. Tiwari, et al., Multiscale modeling-driven synthesis of Cu40Zn24Ni24Ag8Hg4 high entropy alloy with antibacterial properties, Nano-Struct, Nano-Objects 40 (2024) 101391.

[41] N. Xu, Y. Gao, Z. Li, Y. Chen, M. Liu, J. Jia, et al., Immunoregulatory hydrogel decorated with Tannic acid/Ferric ion accelerates diabetic wound healing *via* regulating macrophage polarization, Chem. Eng. J. 466 (2023) 143173.

[42] C. Dong, W. Feng, W. Xu, L. Yu, H. Xiang, Y. Chen, et al., The coppery age: copper (Cu)-involved nanotheranostics, Adv. Sci. 7 (21) (2020) 2001549.

[43] Y. Chen, X. Yang, K. Li, J. Feng, X. Liu, Y. Li, et al., Phenolic ligand–metal charge transfer induced copper nanozyme with reactive oxygen species-scavenging ability for chronic wound healing, ACS Nano 18 (9) (2024) 7024–7036.

[44] Y. Zhang, K. Li, L. Shen, L. Yu, T. Ding, B. Ma, et al., Metal phenolic nanodressing of porous polymer scaffolds for enhanced bone regeneration *via* interfacial gating growth factor release and stem cell differentiation, ACS Appl. Mater. Interfaces 14 (1) (2022) 268–277.

[45] Z. Liu, X. Bian, L. Luo, Å.K. Björklund, L. Li, L. Zhang, et al., Spatiotemporal single-cell roadmap of human skin wound healing, Cell Stem Cell 32 (2024) 1–20.

[46] M. Wen, T. Wang, N. Li, Y. Wu, L. Zhang, Y. Xue, et al., Polyphenol-copper derived self-cascade nanozyme hydrogel in boosting oxygenation and robust revascularization for tissue regeneration, Adv. Funct. Mater. 34 (40) (2024) 2403634.